ADVANCED MATERIALS
www.advmat.de

A Van der Waals Interface Hosting Two Groups of Magnetic Skyrmions

Yingying Wu, Brian Francisco, Zhijie Chen, Wei Wang, Yu Zhang, Caihua Wan, Xiufeng Han, Hang Chi, Yasen Hou, Alessandro Lodesani, Gen Yin, Kai Liu, Yong-tao Cui, Kang L. Wang, and Jagadeesh S. Moodera**

Multiple magnetic skyrmion phases add an additional degree of freedom for skyrmion-based ultrahigh-density spin memory devices. Extending the field to 2D van der Waals magnets is a rewarding challenge, where the realizable degree of freedoms (e.g., thickness, twist angle, and electrical gating) and high skyrmion density result in intriguing new properties and enhanced functionality. In this work, a van der Waals interface, formed by two 2D ferromagnets $Cr_2Ge_2Te_6$ and Fe_3GeTe_2 with a Curie temperature of ≈65 and ≈205 K, respectively, hosting two groups of magnetic skyrmions, is reported. Two sets of topological Hall effect signals are observed below 6s0 K when $Cr_2Ge_2Te_6$ is magnetically ordered. These two groups of skyrmions are directly imaged using magnetic force microscopy, and supported by micromagnetic simulations. Interestingly, the magnetic skyrmions persist in the heterostructure with zero applied magnetic field. The results are promising for the realization of skyrmionic devices based on van der Waals heterostructures hosting multiple skyrmion phases.

1. Introduction

2D magnetism was recently discovered in van der Waals (vdW) ferromagnets[1–3] and antiferromagnets,[4–6] providing unprecedented opportunities for exploring magnetism, and toward spintronic applications in the 2D limit.[7–9] Among all the interface engineered heterostructures based on vdW layered systems, magnetic proximity effect is integral to manipulating spintronic,[10–12] superconducting,[13–15] and topological phenomena.[16–18] Magnetic skyrmions have been well studied due to their nontrivial topology, which leads to many interesting fundamental and dynamical properties.[19–21] These have been reported mostly for noncentrosymmteric single crystals,[22–24] ultrathin epitaxial system,[25,26] and magnetic multilayers.[27–31] Recently Néel-type skyrmions were observed in a vdW ferromagnet interfaced with an oxidized layer[32] or a transition metal dichalcogenide[33] with a control of the skyrmion phase through tuning of the ferromagnet thickness. Furthermore, with a variety of vdW magnets, skrymions phase could be created in their new interfaces with unique properties.

Materials hosting multiple skyrmion phases add richness to the field, with an additional degree of freedom in designing

Y. Wu, H. Chi, Y. Hou, A. Lodesani, J. S. Moodera
Francis Bitter Magnet Laboratory and Plasma Science and Fusion Center
Massachusetts Institute of Technology
Cambridge, MA 02139, USA
E-mail: yywu@mit.edu; moodera@mit.edu

B. Francisco, Y.-t. Cui
Department of Physics and Astronomy
University of California
Riverside, CA 92521, USA

Z. Chen, G. Yin, K. Liu
Department of Physics
Georgetown University
Washington, D.C. 20057, USA

The ORCID identification number(s) for the author(s) of this article can be found under https://doi.org/10.1002/adma.202110583.

DOI: 10.1002/adma.202110583

W. Wang
Key Laboratory of Flexible Electronics & Institute of Advanced Materials
Jiangsu National Synergetic Innovation Center for Advanced Materials
Nanjing Tech University
Nanjing 211816, China

Y. Zhang, C. Wan, X. Han
Institute of Physics
Chinese Academy of Sciences
Beijing 100190, China

H. Chi
U.S. Army CCDC Army Research Laboratory
Adelphi, MD 20783, USA

K. L. Wang
Department of Electrical and Computer Engineering
University of California
Los Angeles, Los Angeles, CA 90095, USA

J. S. Moodera
Physics Department
Massachusetts Institute of Technology
Cambridge, MA 02139, USA

devices. Such a degree of freedom adds value as a means to lower the error rate in racetrack memories with skyrmions as information carriers.[34,35] Multiple skyrmion phases have been reported in FeGe grown on Si(111) at low temperatures[36] and in Ir/Fe/Co/Pt multilayers.[34] Different from these thin film systems, vdW heterostructures possess well defined and ordered atomic layer range of thicknesses, atomically sharp interfaces and easy electrical field control. Forming a heterostructure of two vdW ferromagnets allows breaking of inversion symmetry at the interface,[20] with skyrmions expected inside both these two ferromagnetic layers in the context of strong spin orbit coupling. This approach enables imprinting of skyrmions to neighboring layers in heterostructures. By stacking 2D ferromagnetic layers, the different groups of skyrmions can be formed vertically, adding a new degree of freedom to skyrmion-based spintronic devices.

In this work, we demonstrate that a vdW interface, that is, $Fe_3GeTe_2/Cr_2Ge_2Te_6$ (FGT/CGT) interface, can host two groups of magnetic skyrmions. The initial signature for this comes from the observation of the topological Hall effect (THE). Below the Curie temperature T_C (≈65 K) of CGT, Hall resistivity shows two sets of kinks, due to the magnetic skyrmion phase formation on CGT and FGT sides. Above 60 K, there is only one set of kinks seen in the Hall resistivity, likely arising from the skyrmion phase on the FGT side. To ascertain and understand the origin of THE, magnetic force microscopy (MFM) was used to image the skyrmion lattice directly, consistent with our micromagnetic simulation results. These observations could provide a new platform for designing a robust skyrmion-based memory and computing architectures by coding the information in multiple groups of skyrmions.

2. Results

2.1. Ferromagnetic Fe_3GeTe_2 and $Cr_2Ge_2Te_6$ Thin Layers

CGT is a soft, 2D layered ferromagnetic crystal, with rhombohedral structure and vdW stacking of hexagonal layers. As illustrated in **Figure 1**a, a layer of Cr atoms is sandwiched between two Ge–Te layers, forming a monolayer of CGT. Its lattice parameters are a = 6.826 Å and c = 20.531 Å. Among the 2D magnets, FGT is a ferromagnet with a strong perpendicular magnetic anisotropy. Bulk FGT consists of weakly bonded Fe_3Ge layers that alternate with two Te layers with a space group $P6_3mmc$, as shown in Figure 1b, with lattice parameters a = 3.991 Å and c = 16.333 Å.[37] For both pristine CGT and FGT crystals, the inversion symmetry is preserved inside the bulk. However, by forming an interface between these two materials, the inversion symmetry is broken. With spin-orbit coupling present, Dzyaloshinskii–Moriya interaction (DMI) is induced at the interface as shown in Figure 1c, both at FGT and CGT interfacial layers. The DMI between two atomic spins S_1 and S_2 can be expressed as: $H_{DM} = -D_{12} \cdot (S_1 \times S_2)$.

The crystal structure of grown CGT crystal was analyzed by using X-ray diffraction studies as depicted in Figure 1d. Typical peaks corresponding to the (003), (006), and (0012) planes in CGT were observed. These peaks indicate that the layered CGT crystal with good quality is achieved. The T_C for CGT was around 65 K, as seen from magnetization measurement using a magnetometer (Figure 1e). The ferromagnetic order in CGT develops at low temperatures upon cooling down both without and with an out-of-plane magnetic field. The magnetic hysteresis is shown in Figure 1f, where the ferromagnetism disappears above 65 K. Compared to CGT, FGT has a much higher T_C of around 205 K, as shown in Figure 1g.

2.2. Two Sets of THE Signals

THE can arise from the accumulated Berry phase acquired by electrons in the adiabatic limit as they encounter a skyrmion along their path. However, recent experiments offered an alternative interpretation of the topological Hall effect reported in topological insulator heterostructures; they attribute the topological Hall signals to the overlapping of two anomalous Hall signals with opposite signs. A similar reasoning was used to explain the topological Hall-like signatures (one peak and one dip) in $SrTiO_3/SrRuO_3/SrTiO_3$ heterostructures.[38] In such a scenario, the competing anomalous Hall signals contributing to topological Hall-like signatures originate either from the coexisting surface and bulk magnetic phases in the magnetic topological insulator system,[39] or two interfaces in the heterostructures. As opposed to previous systems, this current FGT/CGT bilayer system might facilitate the demonstration of THE for three reasons: 1) only one interface is formed between the two materials; 2) two sets of kinks, a signature for THE at both sides of an interface, are observed when the temperature is lower than the T_C of CGT; and 3) skyrmions are imaged directly by MFM.

In the transport measurements, CGT/FGT thin films were transferred onto prepared Hall-bar bottom electrodes under a microscope (see Section S1, Supporting Information for device images) inside the glove box (N_2 atmosphere) (details of the sample assembly can be found in Section S2, Supporting Information), and the resistivity was measured using lock-in technique. The CGT layers for the transport measurement have a thickness between 30 and 40 nm, which are relatively insulating compared to metallic FGT layers. Magnetic field was applied perpendicular to the sample plane. As shown in **Figure 2**a, 20-layer (20L) FGT exhibits square hysteresis loop when the temperature is below 200 K, demonstrating a strong perpendicular magnetic anisotropy. When FGT thickness was reduced to 5L, interface coupling between FGT and CGT gave rise to pronounced peaks and dips near the magnetic transition edge, the signature of THE. Different from previously reported systems, two sets of THEs (as indicated by blue and orange circles in Figure 2b) are observed in this heterostructure of two ferromagnets. Similar results from another heterostructure with 5L FGT can be found in Section S3, Supporting Information.

The topological Hall resistivity value is related to carrier density n, and an effective field B_{eff} generated by skyrmion lattice ($\rho_{xy}^{THE} \approx \frac{1}{ne} B_{eff}$).[40] The different magnitude of the topological Hall resistivity value indicates two groups of skyrmions with different sizes. These two sets of THEs coexist when the temperature is below the T_C of CGT. One set indicated by the orange circles vanishes at 60 K and above, is attributable to the disappearance of ferromagnetic order in CGT with increasing

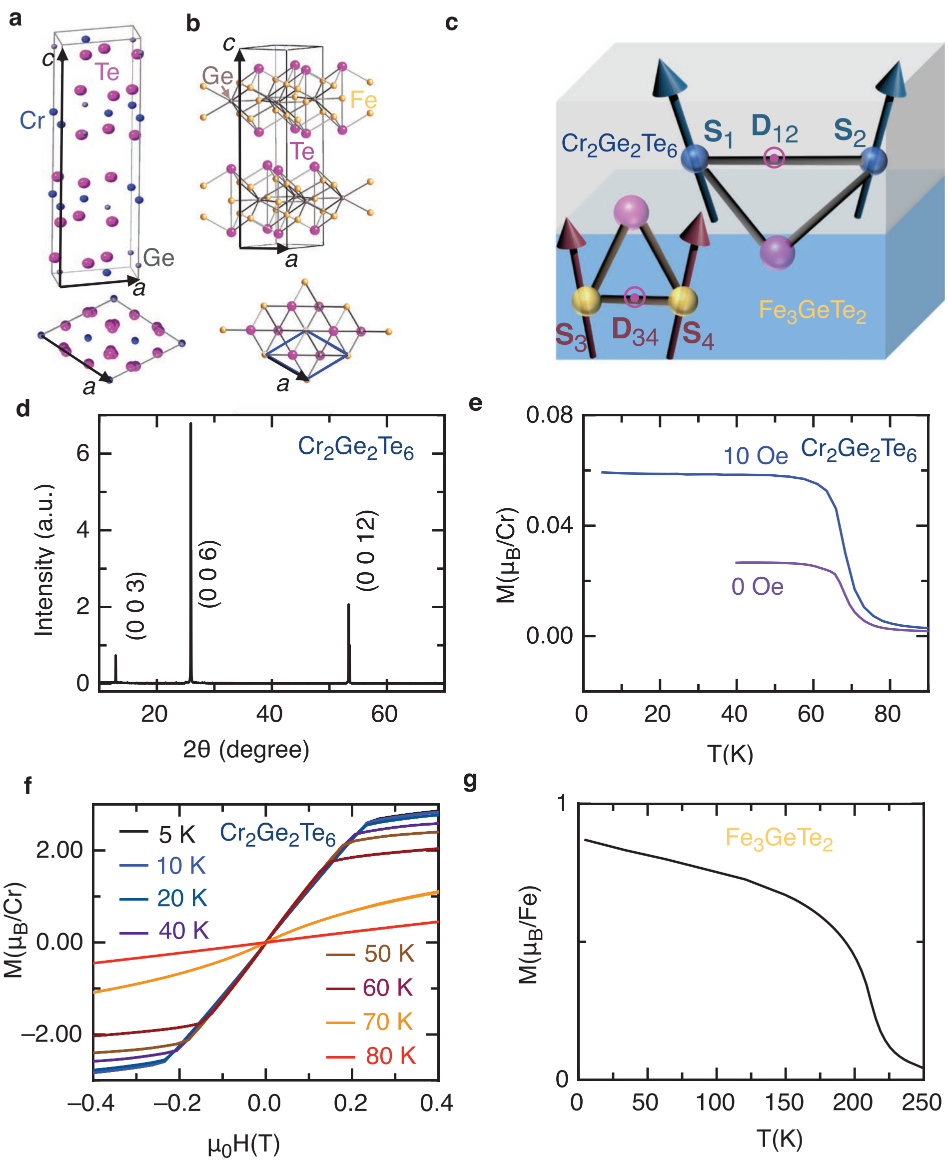

Figure 1. Structure and magnetic properties in FGT and CGT crystals. a) Crystal structure of CGT. Side view and top view for the rhombohedral structure. b) Crystal structure of FGT. c) DMI is induced at the interface of CGT and FGT. d) X-ray diffraction pattern of CGT indicating a high-quality crystal. e) The temperature-dependent magnetization profile of CGT under zero-field-cooled and field-cooled (out-of-plane applied magnetic field $H = 10$ Oe) conditions, revealing a T_C of ≈65 K. f) Magnetic hysteresis profile of CGT at selected temperatures with applied magnetic field $H//c$-axis displaying an anisotropy field of ≈220 mT at 20 K. g) The temperature-dependent magnetization profile of FGT under zero-field cooling condition, indicating a T_C of ≈205 K.

temperature. Noted that this THE is only observed in the CGT/5L FGT sample. The absence of THE in the heterostructure with thicker FGT can be due to the high carrier density. With larger carrier density in thicker FGT samples, the topological Hall resistivity is dwarfed in comparison. For example, for 20L FGT at 20 K, the estimated topological Hall resistivity contribution is less than $10^{-3}\,\Omega$ (details of the carrier density can be found in Section S4, Supporting Information), assuming a skyrmion lattice with a size of 100 nm. This resistivity value is more than two orders of magnitude smaller than the anomalous Hall resistivity, and thus tends to be buried in the anomalous Hall signals.

2.3. Magnetic Skyrmions Directly Imaged by MFM

To further examine the origin of THE arising at the FGT/CGT interface, we performed low-temperature MFM measurements under applied magnetic fields (resolution of the MFM measurement can be found in Section S5, Supporting Information). In MFM, the magnetic stray field from nanoscale features is detected by a scanning nanoscale magnetic tip (**Figure 3**a). Note that in our topological Hall resistivity, two sets of kinks were observed, attributable to magnetic skyrmions on the FGT side and the CGT side, respectively (Figure 3b). In our MFM setup, the MFM signal characterizes the second-order derivative of

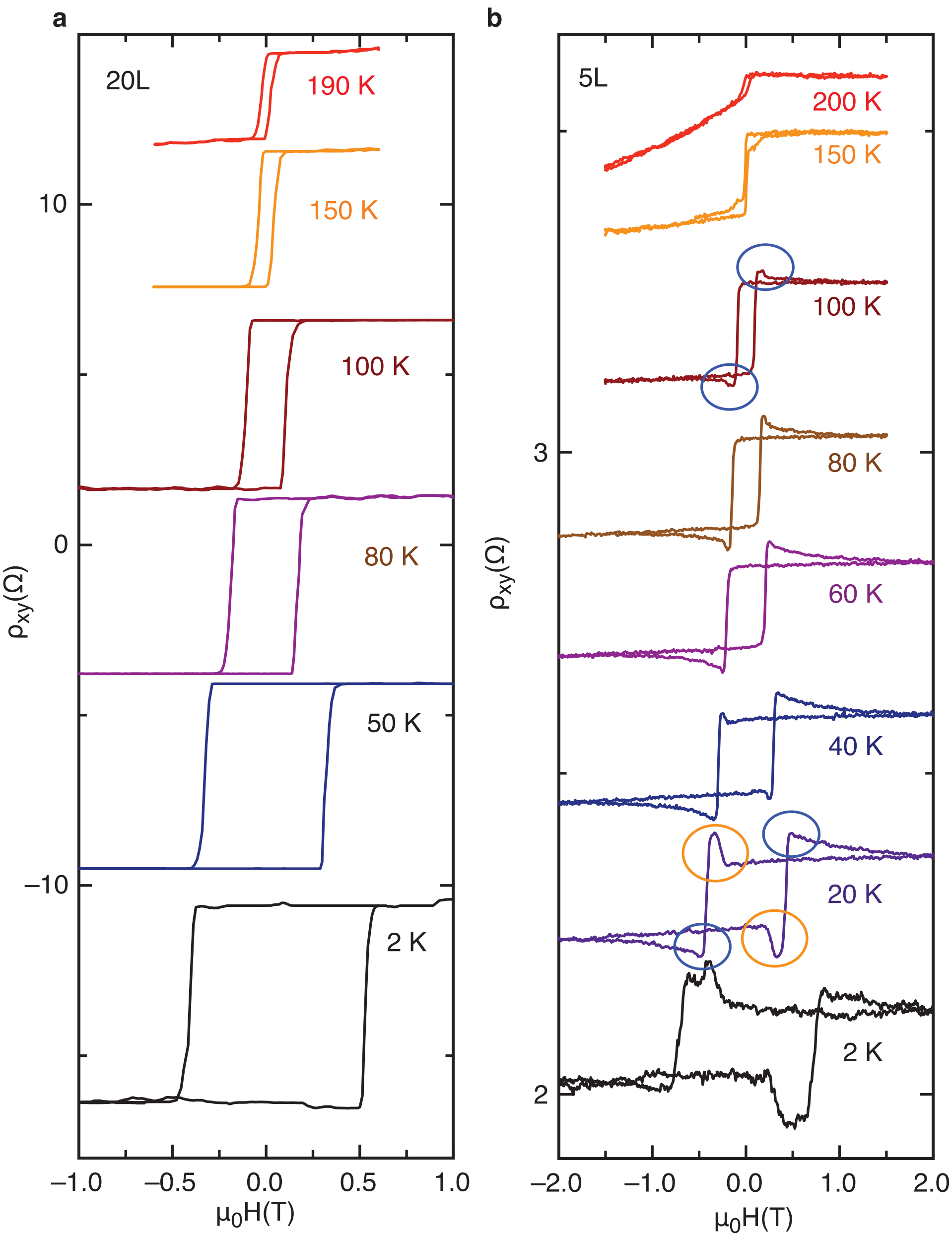

Figure 2. Topological Hall effect in the $Cr_2Ge_2Te_6$/Fe_3GeTe_2 heterostructure. a,b) Hall resistivity (shifted for clarity) of a CGT/FGT heterostructure with different FGT thicknesses of 20L (a), and 5L (b). A magnetic field was applied perpendicular to the sample plane, that is, along the *c*-axis. A square hysteresis loop indicates the perpendicular magnetic anisotropy. Peaks and dips appear in the heterostructure with 5L FGT, signifying the existence of topological Hall effect.

the out-of-plane component of the stray field, that is, d^2H_z/dz^2. For the samples with an out-of-plane magnetization, MFM responds to both the interior of magnetic domains and the domain walls. Figure 3c shows a series of MFM images taken on the CGT/FGT device (device measured in Figure 2b) with applied perpendicular magnetic fields at 20 K. As the field increases from zero, the image captures labyrinth domains. Upon increasing the field to 160 mT, skyrmionic features start to form as indicated by the yellow circles in Figure 3c. At 200 mT, skyrmion lattice with a size of ≈130 nm was directly imaged. This skyrmion lattice disappears and the sample enters into a uniform single domain as the field is increased to 250 mT (see Section S6, Supporting Information for skyrmion lattice at larger magnetic fields). These observed magnetic skyrmions are expected to occur at the interface close to the CGT side for three reasons: 1) with CGT on top of FGT, MFM signals would be dominated by the magnetic fields generated by the CGT layer, 2) the magnetic signal from 5L FGT under multilayer CGT is too weak to be observed (or screened), and 3) the formation of magnetic skyrmion lattices exactly matches the magnetic field which leads to the development of THE on the CGT side (the dip at a positive magnetic field in Figures 2b and 3b).

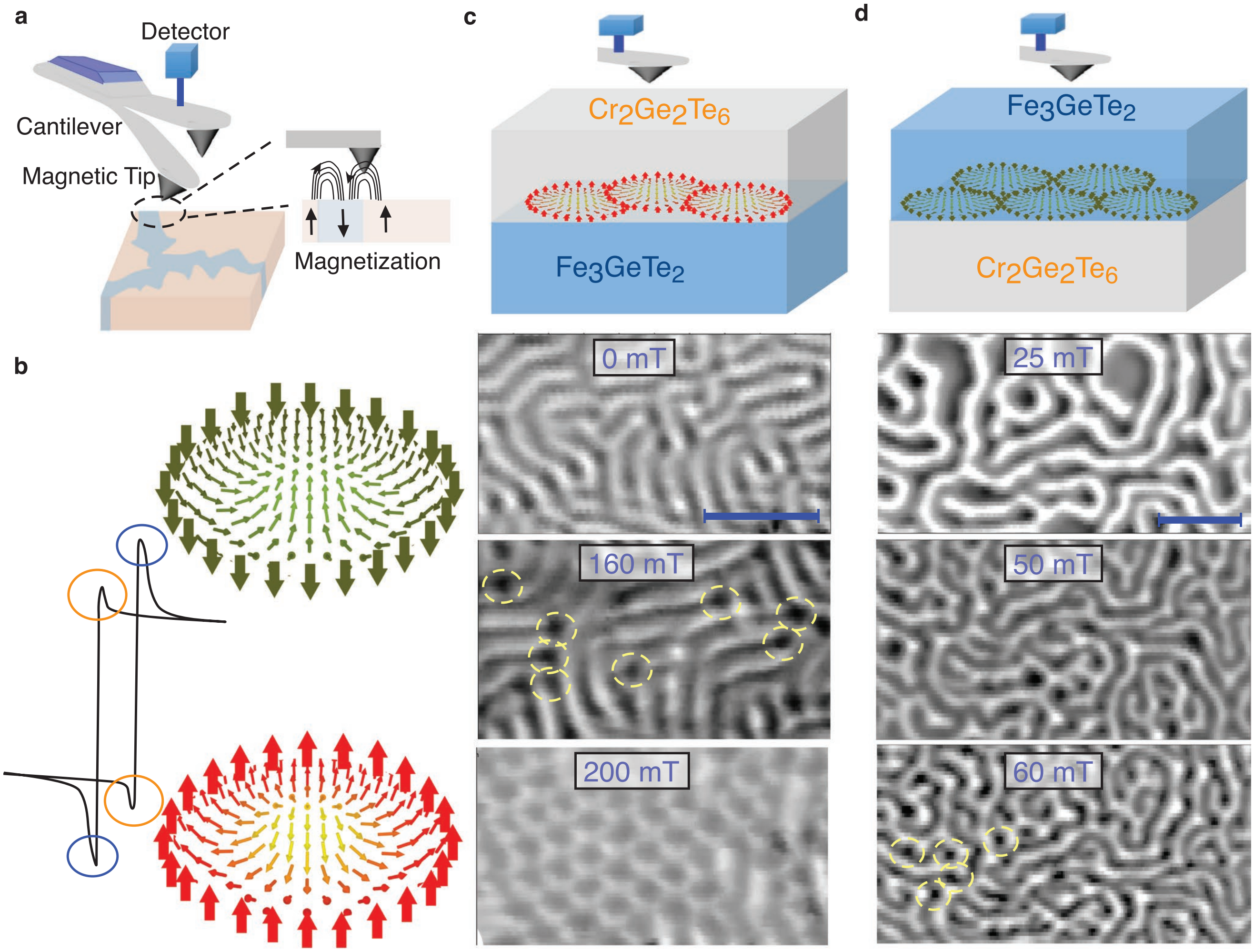

Figure 3. Skyrmions at both sides of $Fe_3GeTe_2/Cr_2Ge_2Te_6$ interface imaged by MFM. a) Schematic illustration of MFM measurements. b) Two sets of THE signals observed for temperatures lower than 60 K. The blue circles signifying THE on the FGT side and orange circles signifying THE on the CGT side. The peak and dip features of THE resistivity indicating the skyrmions with opposite polarity. c) Skyrmion lattice observed on the FGT side on the CGT side with a magnetic field of 200 mT and a temperature of 20 K. Scale bar: 1 µm. d) Skyrmions on the FGT side start to appear with a magnetic field of 50 mT at a temperature of 100 K. Scale bar: 1 µm.

With a reversed sample structure, that is, with the FGT layer on top of the CGT layer, the MFM measurements show domain images on the FGT side in Figure 3d. At 100 K, similar labyrinth domains are captured at 25 mT but with a larger domain width, compared to the CGT case at 20 K. When the field further increases, skyrmions start to show up, as indicated by the yellow circles. The skyrmion size is estimated to be ≈180 nm (100 K and 60 mT), which further decreases as the temperature goes down. Images of the skyrmion lattice at a lower temperature on the FGT side after Fourier analysis can be found in Section S7, Supporting Information.

The skyrmion lattice in the CGT/FGT heterostructure develops by controlling the magnetic field. When sweeping from a negative field (−2 T), the CGT magnetization first saturates at 20 K, and then skyrmions develop at ≈−50 mT (**Figure** 4a). Interestingly, these skyrmions seem to persist when the applied magnetic field is turned off. Emergence of magnetic skyrmions at 0 T has been predicted to be a possible signature of Moiré skyrmions.[41] The real reason and mechanism of zero-field magnetic skyrmions is not clear in our case at present. One should also consider the role of the exchange coupling between CGT and FGT, where the FGT layer provides an extra effective field. When the magnetic field was further increased to 120 mT, skyrmion lattice emerged forming a hexagonal pattern. Further increasing the magnetic field to 140 mT, the skyrmions are switched due to the flip of the tip magnetization driven by the external magnetic field.

The skyrmion size can be extracted from the THE and the skyrmion images by MFM measurements (Figure 4b). The skyrmion size on both sides of the heterostructure decreases by lowering the temperature. The error bars in the MFM measurement (dots and squares with dashed lines) are due to the variation of the skyrmion size under applied magnetic field. The skyrmion size extracted from the THE (dots and squares with solid lines) offers an order of magnitude estimate (details of the size extraction can be found in Section S8, Supporting

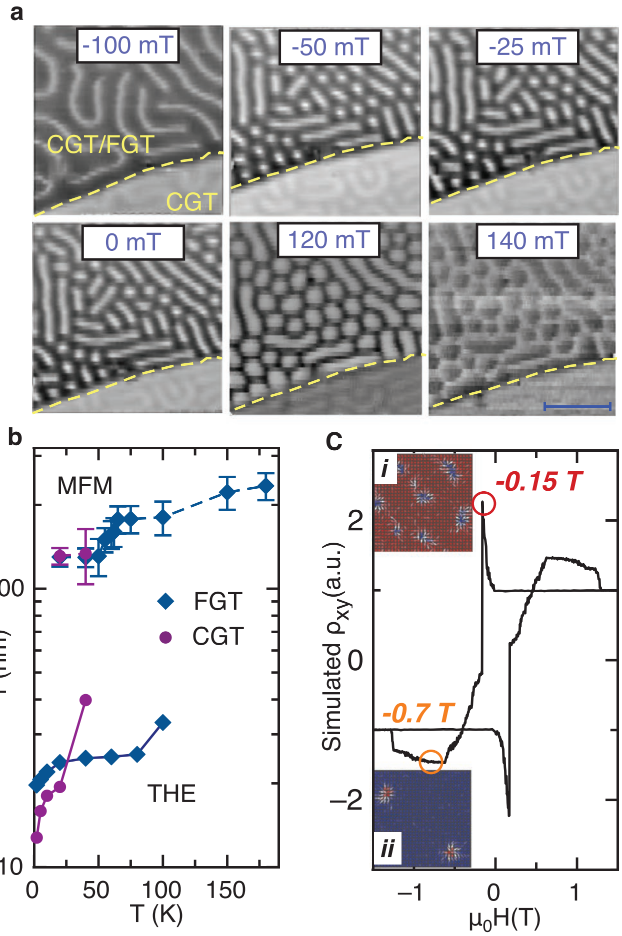

Figure 4. Magnetic skyrmions showing up as a function of magnetic field (even at zero field) and skyrmion size dependence on the temperature. a) Skyrmion lattice on the CGT side under various applied magnetic fields at 20 K after subjecting to −2 T. Scale bar: 1 µm. b) Skyrmion size extracted from topological Hall effect (an order-of-magnitude estimate) and from MFM images. The data points with dashed lines are from MFM measurements and the data points with solid lines are from topological Hall effects. c) Micromagnetic simulations for magnetic skyrmions at FGT/CGT interface. i,ii) Skyrmions at the interface with fields of −0.15 T (i) and −0.7 T (ii).

Information), which is around one order of magnitude smaller than that from MFM measurement.

The skyrmion size under MFM is around 100 nm. At present, most of the magnetic domain sizes of commercial hard disk drives are less than 100 nm. Follow-up research can be carried out to further reduce the skyrmion size in vdW heterostructures. One example is through electric gating, where the magnetic anisotropy in FGT and CGT can be largely modified[2,42] and thus the skyrmion size can be tuned. Another example is searching for a new type of skyrmion in vdW heterostructures, that is, Moiré skyrmion,[41] with a size of tens of nanometers and below.

For an interface formed between CGT and FGT, we can also estimate the DMI energy from the strip domain width. The DMI in FGT is estimated to be, $|D| = 0.31 \pm 0.13$ mJ m^{-2} (details can be found in Section S9, Supporting Information), a value similar to that reported in WTe_2/FGT system,[11] a vdW heterostructure hosting skyrmion lattice (the differences between the skyrmions in the heterostructure and the skyrmion bubbles in the pristine centrosymmetric magnets can be found in Section S10, Supporting Information).

Simualtions using GPU-accelerated micromagnetic simulation program MuMax3[43] were carried out to understand the system. Figure 4c shows two sets of THE signals when considering the topological charges in both the FGT and the interface. Starting from positive saturation and lowering the field to −0.15 T, the first THE peak shows up. This indicates the skyrmion phase at the interface on the CGT side (Figure 4c-i). Further decreasing the field to −0.7 T, skyrmions show up both in the FGT layer and the interface on the FGT side (Figure 4c-ii). Details of the simulation can be found in Section S11, Supporting Information.

3. Conclusion

We have explored the ultrathin FGT/CGT heterostructures as a platform for hosting small and tunable two groups of magnetic skyrmions. In this system, the inversion symmetry breaking near the FGT/CGT interface gives rise to an emergent DMI, thereby creating robust magnetic skyrmions. By harnessing the interface between two vdW ferromagnets, we achieved magnetic skyrmions at two sides of an interface.

The multiple groups of skyrmions in FGT/CGT heterostructures allow versatility when designing and fabricating skyrmion-based devices. Our findings demonstrate imprinting of skyrmions to neighboring layers in 2D heterostructures. By proper design of multilayer 2D magnetic stack, different groups of skyrmions can be formed vertically, adding a new degree of freedom to skyrmion-based spintronic devices. Besides, due to the atomically thin nature of vdW materials and their easy control by electrical gating, one can foresee manipulating the skyrmions on each side with dual electric gating by which the skyrmion phase can be turned on or off. Furthermore, the twist angle between FGT and CGT may be tuned, where a new functionality could be added for manipulating skyrmions in atomically thin vdW heterostructures. With an accurate determination of twist angle between FGT and CGT layers, magnetic skyrmions from DMI or Moiré pattern may be differentiated. This versatile advantage offers a fertile playground for exploring emergent phenomena arising from hybrid interfaces, leading to magnetic skyrmions with additional functionalities.

4. Experimental Section

Growth of FGT and CGT Crystals: High-quality single crystals of FGT were grown by a typical chemical vapor transport method. The stoichiometric amounts of high-purity elements (99.999% Fe, 99.999% Ge, and 99.999% Te from Alfa Aesar) along with 2 mg cm^{-3} iodine the transport agent were placed in a quartz ampoule and sealed under vacuum. The ampoule was further placed in a horizontal two-zone furnace over a temperature gradient from 750 to 700°C and kept at that condition for 2 weeks. The single crystals with a tabular shape in the *ab*-plane grew in the low-temperature zone.

High-quality CGT single crystals were synthesized from high-purity elements (99.99% Cr, 99.99% Ge, and >99.99% Te from Alfa Aesar). A mixture of materials with an optimized ratio of Cr:Ge:Te equivalent to

10:13.5:76.5, was sealed in evacuated quartz ampoules and heated at 1000 °C for 1 day, followed by slow cooling to 450 °C for a period of 90 h.

MFM Measurement: The MFM measurements were performed in a home-built low-temperature scanning probe microscope using commercial MFM probes (Bruker MESPV2) with a spring constant of 3 N m^{-1}, a resonance frequency at ≈75 kHz, and a Co–Cr magnetic coating. MFM images were taken in a constant height mode with the tip scanning plane at ≈100 nm above the sample surface. The MFM signal, the change in the resonance frequency, was measured by a Nanonis SPM controller using a phase-lock loop. The magnetic moment of the probe was nominally in the order of 10^{-16} A m^2.

Magnetotransport Measurement: Hall-bar bottom electrodes with dimension of 3.5 μm × 0.5 μm were fabricated with e-beam lithography for the transport measurements. Systematically altering experimental variables such as temperature and magnetic field, in addition to multiple lock-in amplifiers and sourcemeter enabled comprehensive and high-sensitivity transport measurements in all the devices, using a commercial PPMS from quantum design (2 K, ± 9T).

Supporting Information

Supporting Information is available from the Wiley Online Library or from the author.

Acknowledgements

Y.W. and B.F. contributed equally to this work. The transport measurements in this work are supported by the Army Research Office (ARO) program under contract W911NF-15-1-10561, National Science Foundation (NSF) with Award Nos. 1935362 and 1909416, CIQM-NSF DMR-1231319, and ARO grant W911NF-20-2-0061. H.C. was sponsored by the Army Research Laboratory under cooperative agreement No. W911NF-19-2-0015. The authors are also grateful to the support from the NSF (DMR-1411085) and Department of Energy, Office of Science under Award No. DE-SC0020221. MFM measurements are supported by NSF DMR-2145735. Micromagnetic simulations are supported by NSF DMR 2005108.

Note: The equal contribution statement was added on April 21, 2022, after initial publication online. The article numbers for refs. [31] and [36] were also corrected.

Conflict of Interest

The authors declare no conflict of interest.

Data Availability Statement

The data that support the findings of this study are available from the corresponding author upon reasonable request.

Keywords

2D magnetism, interface coupling, layered magnets, magnetic skyrmions

Received: December 27, 2021
Revised: January 26, 2022
Published online: March 10, 2022

[1] C. Gong, L. Li, Z. Li, H. Ji, A. Stern, Y. Xia, T. Cao, W. Bao, C. Wang, Y. Wang, Z. Q. Qiu, R. J. Cava, S. G. Louie, J. Xia, X. Zhang, *Nature* **2017**, *546*, 265.
[2] Y. Deng, Y. Yu, Y. Song, J. Zhang, N. Z. Wang, Z. Sun, Y. Yi, Y. Z. Wu, S. Wu, J. Zhu, J. Wang, X. H. Chen, Y. Zhang, *Nature* **2018**, *563*, 94.
[3] Z. Fei, B. Huang, P. Malinowski, W. Wang, T. Song, J. Sanchez, W. Yao, D. Xiao, X. Zhu, A. F. May, W. Wu, D. H. Cobden, J. Chu, X. Xu, *Nat. Mater.* **2018**, *17*, 778.
[4] B. Huang, G. Clark, E. Navarro-Moratalla, D. R. Klein, R. Cheng, K. L. Seyler, D. Zhong, E. Schmidgall, M. A. McGuire, D. H. Cobden, W. Yao, *Nature* **2017**, *546*, 270.
[5] X. Wang, K. Du, Y. Y. F. Liu, P. Hu, J. Zhang, Q. Zhang, M. H. S. Owen, X. Lu, C. K. Gan, P. Sengupta, C. Kloc, Q. Xiong, *2D Mater.* **2016**, *3*, 031009.
[6] J.-U. Lee, S. Lee, J. H. Ryoo, S. Kang, T. Y. Kim, P. Kim, C.-H. Park, J.-G. Park, H. Cheong, *Nano Lett.* **2016**, *16*, 7433.
[7] K. S. Burch, D. Mandrus, J.-G. Park, *Nature* **2018**, *563*, 47.
[8] A. Avsar, H. Ochoa, F. Guinea, B. Özyilmaz, B. Van Wees, I. J. Vera-Marun, *Rev. Mod. Phys.* **2020**, *92*, 021003.
[9] J. F. Sierra, J. Fabian, R. K. Kawakami, S. Roche, S. O. Valenzuela, *Nat. Nanotechnol.* **2021**, *16*, 856.
[10] C. Tang, Z. Zhang, S. Lai, Q. Tan, W.-b. Gao, *Adv. Mater.* **2020**, *32*, 1908498.
[11] Y. Wu, G. Yin, L. Pan, A. J. Grutter, Q. Pan, A. Lee, D. A. Gilbert, J. A. Borchers, W. Ratcliff, A. Li, X. Han, K. L. Wang, *Nat. Electron.* **2020**, *3*, 604.
[12] A. Dankert, S. P. Dash, *Nat. Commun.* **2017**, *8*, 16093.
[13] M. Kim, G.-H. Park, J. Lee, J. H. Lee, J. Park, H. Lee, G.-H. Lee, H.-J. Lee, *Nano Lett.* **2017**, *17*, 6125.
[14] Y. Wu, J. J. He, T. Han, S. Xu, Z. Wu, J. Lin, T. Zhang, Y. He, N. Wang, *Phys. Rev. B* **2019**, *99*, 121406.
[15] F. Lüpke, D. Waters, C. Sergio, M. Widom, D. G. Mandrus, J. Yan, R. M. Feenstra, B. M. Hunt, *Nat. Phys.* **2020**, *16*, 526.
[16] S. Kezilebieke, M. N. Huda, V. Vaňo, M. Aapro, S. C. Ganguli, O. J. Silveira, S. Głodzik, A. S. Foster, T. Ojanen, P. Liljeroth, *Nature* **2020**, *588*, 424.
[17] J. Island, X. Cui, C. Lewandowski, J. Khoo, E. Spanton, H. Zhou, D. Rhodes, J. Hone, T. Taniguchi, K. Watanabe, L. S. Levitov, M. P. Zaletel, A. F. Young, *Nature* **2019**, *571*, 85.
[18] F. Hellman, A. Hoffmann, Y. Tserkovnyak, G. S. Beach, E. E. Fullerton, C. Leighton, A. H. MacDonald, D. C. Ralph, D. A. Arena, H. A. Dürr, P. Fischer, *Rev. Mod. Phys.* **2017**, *89*, 025006.
[19] N. Nagaosa, Y. Tokura, *Nat. Nanotechnol.* **2013**, *8*, 899.
[20] A. Fert, V. Cros, J. Sampaio, *Nat. Nanotechnol.* **2013**, *8*, 152.
[21] A. Fert, N. Reyren, V. Cros, *Nat. Rev. Mater.* **2017**, *2*, 17031.
[22] S. Mühlbauer, B. Binz, F. Jonietz, C. Pfleiderer, A. Rosch, A. Neubauer, R. Georgii, P. Böni, *Science* **2009**, *323*, 5916.
[23] X. Yu, Y. Onose, N. Kanazawa, J. H. Park, J. Han, Y. Matsui, N. Nagaosa, Y. Tokura, *Nature* **2010**, *465*, 7300.
[24] F. Jonietz, S. Mühlbauer, C. Pfleiderer, A. Neubauer, W. Münzer, A. Bauer, T. Adams, R. Georgii, P. Böni, R. A. Duine, K. Everschor, M. Garst, A. Rosch, *Science* **2010**, *330*, 6011.
[25] L. Wang, Q. Feng, Y. Kim, R. Kim, K. H. Lee, S. D. Pollard, Y. J. Shin, H. Zhou, W. Peng, D. Lee, W. Meng, H. Yang, J. H. Han, M. Kim, Q. Lu, T. W. Noh, *Nat. Mater.* **2018**, *17*, 1087.
[26] S. Woo, K. Litzius, B. Krüger, M.-Y. Im, L. Caretta, K. Richter, M. Mann, A. Krone, R. M. Reeve, M. Weigand, P. Agrawal, I. Lemesh, M. Mawass, P. Fisher, M. Klaui, G. S. D. Beach, *Nat. Mater.* **2016**, *15*, 501.
[27] W. Jiang, P. Upadhyaya, W. Zhang, G. Yu, M. B. Jungfleisch, F. Y. Fradin, J. E. Pearson, Y. Tserkovnyak, K. L. Wang, O. Heinonen, G. E. T. V. Velthuis, A. Hoffmann, *Science* **2015**, *349*, 6245.
[28] W. Li, I. Bykova, S. Zhang, G. Yu, R. Tomasello, M. Carpentieri, Y. Liu, Y. Guang, J. Gräfe, M. Weigand, D. M. Burn, G. Laan, T. Hesjedal, Z. Yan, J. Feng, C. Wan, J. Wei, X. Wang, X. Zhang, H. Xu, C. Guo, H. Wei, G. Finocchio, X. Han, G. Schütz, *Adv. Mater.* **2019**, *31*, 1807683.
[29] R. Wiesendanger, *Nat. Rev. Mater.* **2016**, *1*, 16044.

[30] D. Maccariello, W. Legrand, N. Reyren, K. Garcia, K. Bouzehouane, S. Collin, V. Cros, A. Fert, *Nat. Nanotechnol.* **2018**, *13*, 233.
[31] D. A. Gilbert, B. B. Maranville, A. L. Balk, B. J. Kirby, P. Fischer, D. T. Pierce, J. Unguris, J. A. Borchers, K. Liu, *Nat. Commun.* **2015**, *6*, 8462.
[32] T.-E. Park, L. Peng, J. Liang, A. Hallal, F. S. Yasin, X. Zhang, K. M. Song, S. J. Kim, K. Kim, M. Weigand, G. Schutz, *Phys. Rev. B* **2021**, *103*, 104410.
[33] Y. Wu, S. Zhang, J. Zhang, W. Wang, Y. L. Zhu, J. Hu, G. Yin, K. Wong, C. Fang, C. Wan, X. Han, Q. Shao, T. Taniguchi, K. Watanabe, J. Zang, Z. Mao, X. Zhang, K. L. Wang, *Nat. Commun.* **2020**, *11*, 3860.
[34] A.-O. Mandru, O. Yıldırım, R. Tomasello, P. Heistracher, M. Penedo, A. Giordano, D. Suess, G. Finocchio, H. J. Hug, *Nat. Commun.* **2020**, *11*, 6365.
[35] D. Suess, C. Vogler, F. Bruckner, P. Heistracher, C. Abert, *AIP Adv.* **2018**, *8*, 115301.
[36] A. S. Ahmed, J. Rowland, B. D. Esser, S. R. Dunsiger, D. W. McComb, M. Randeria, R. K. Kawakami, *Phys. Rev. Mater.* **2018**, *2*, 041401(R).
[37] J. Yi, H. Zhuang, Q. Zou, Z. Wu, G. Cao, S. Tang, S. Calder, P. Kent, D. Mandrus, Z. Gai, *2D Mater.* **2016**, *4*, 011005.
[38] G. Kimbell, P. M. Sass, B. Woltjes, E. K. Ko, T. W. Noh, W. Wu, J. W. Robinson, *Phys. Rev. Mater.* **2020**, *4*, 054414.
[39] K. M. Fijalkowski, M. Hartl, M. Winnerlein, P. Mandal, S. Schreyeck, K. Brunner, C. Gould, L. W. Molenkamp, *Phys. Rev. X* **2020**, *10*, 011012.
[40] A. Neubauer, C. Pfleiderer, B. Binz, A. Rosch, R. Ritz, P. Niklowitz, P. Böni, *Phys. Rev. Lett.* **2009**, *102*, 186602.
[41] Q. Tong, F. Liu, J. Xiao, W. Yao, *Nano Lett.* **2018**, *18*, 7194.
[42] I. A. Verzhbitskiy, H. Kurebayashi, H. Cheng, J. Zhou, S. Khan, Y. P. Feng, G. Eda, *Nat. Electron.* **2020**, *3*, 460.
[43] A. Vansteenkiste, J. Leliaert, M. Dvornik, M. Helsen, F. Garcia-Sanchez, B. Van Waeyenberge, *AIP Adv.* **2014**, *4*, 107133.